Three Isomeric Zn(II)−Sn(IV)−Zn(II) Porphyrin-Triad-Based Supramolecular Nanoarchitectures for the Morphology-Dependent Photocatalytic Degradation of Methyl Orange

Nirmal Kumar Shee and Hee-Joon Kim*

Read Online

ACCESS | Metrics & More | Article Recommendations | SI Supporting Information

ABSTRACT: Three isomeric Zn(II)−Sn(IV)−Zn(II) porphyrin-based triads (**T2**, **T3**, and **T4**) were synthesized by the reaction of common Zn(II) porphyrins (**ZnL**) with different Sn(IV) porphyrins (**SnP^n**). The Sn(IV) porphyrin precursors differ with respect to the position of the pyridyl-N atoms. All compounds were characterized by ^{1}H NMR, UV−vis, fluorescence spectroscopy, electrospray ionization−mass spectrometry, and field-emission scanning electron microscopy measurements. In these structures, the intramolecular cooperative metal−ligand coordination of the 3-pyridyl nitrogen in **SnP^3** with axial **ZnL** and the $\pi-\pi$ interactions between the adjacent porphyrin triad are the determining factors affecting the nanostructures of **T3**. Owing to the geometrical constraints of the **SnP^2** center, this type of interaction is not possible for **T2**. Therefore, only the $\pi-\pi$ interactions affect the self-assembly process. In the case of **SnP^4**, intermolecular coordinative interactions and then $\pi-\pi$ interactions are responsible for the nanostructure of **T4**. The morphology-dependent photocatalytic degradation of methyl orange (MO) dye in aqueous solution under visible light irradiation was observed for these photocatalysts, and the degradation ratio of MO varied from 76 to 94% within 100 min. Nanorod-shaped **T3** exhibited higher performance compared to nanosphere **T2** and nanoflake **T4**.
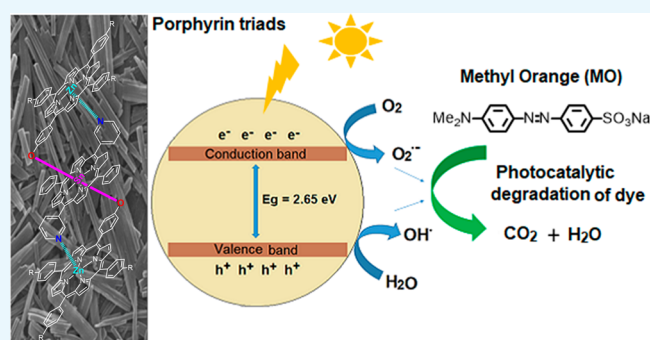
INTRODUCTION

Highly ordered and well-defined nanomaterials have drawn tremendous attention in the fields of applied and materials chemistry owing to their varied applications, such as the conversion and storage of solar energy,[1] catalysis,[2] sensing,[3] molecular recognition,[4] and biomedicine.[5] In addition, these materials have high surface areas,[6] excellent corrosion resistance,[7] high electrical conductivity,[8] outstanding optoelectronic properties,[9] and high thermal stability[10] compared to their parent constituents. Thus, a large number of building blocks have been used to construct nano- and microstructured nanomaterials having well-defined shapes and dimensions.[11−14] Porphyrinoids (free porphyrin or metalloporphyrin compounds) are emerging building blocks for the fabrication of self-assembled functional nanomaterials having light-harvesting properties or charge-transfer functionality.[15−18] In general, free porphyrin or metalloporphyrin compounds self-assemble and form large aggregates in solution. Several intermolecular noncovalent interactions (for example, hydrogen bonding, van der Waals, $\pi-\pi$ stacking, ligand coordination, electrostatic, hydrophobic, and hydrophilic interactions) are responsible for the self-assembly of porphyrinoid compounds.[19−23] The morphology of these nanostructures is not always regular, making them unsuitable for practical applications. Therefore,

the design and construction of novel nanoarchitectures having definite sizes, shapes, and dimensions is challenging. Sn(IV) porphyrin compounds have been widely used as building blocks in the construction of nanomaterials, including nanofibers,[24] nanotubes,[25] nanosheets,[26] nanorods,[27] and nanocomposites,[28] and these nanoaggregates have applications for the production of hydrogen gas under visible-light irradiation[29] and the photocatalytic degradation of organic dyes in aqueous solution.[30,31] Because of the oxophilic nature of Sn(IV) centers, they form stable six-coordinated complexes with two *trans*-oriented oxyanion ligands (alkoxides or carboxylates) and thus are ideal scaffolds for the construction of supramolecular architectures.[32−38] These compounds have interesting photophysical properties and are diamagnetic. Therefore, structural information can be obtained from the Sn nuclei, which are NMR-active. To date, a large number of methods, including ionic self-assembly,[39] reprecipitation,[40] sonication,[41] metal−
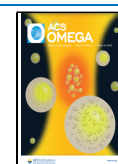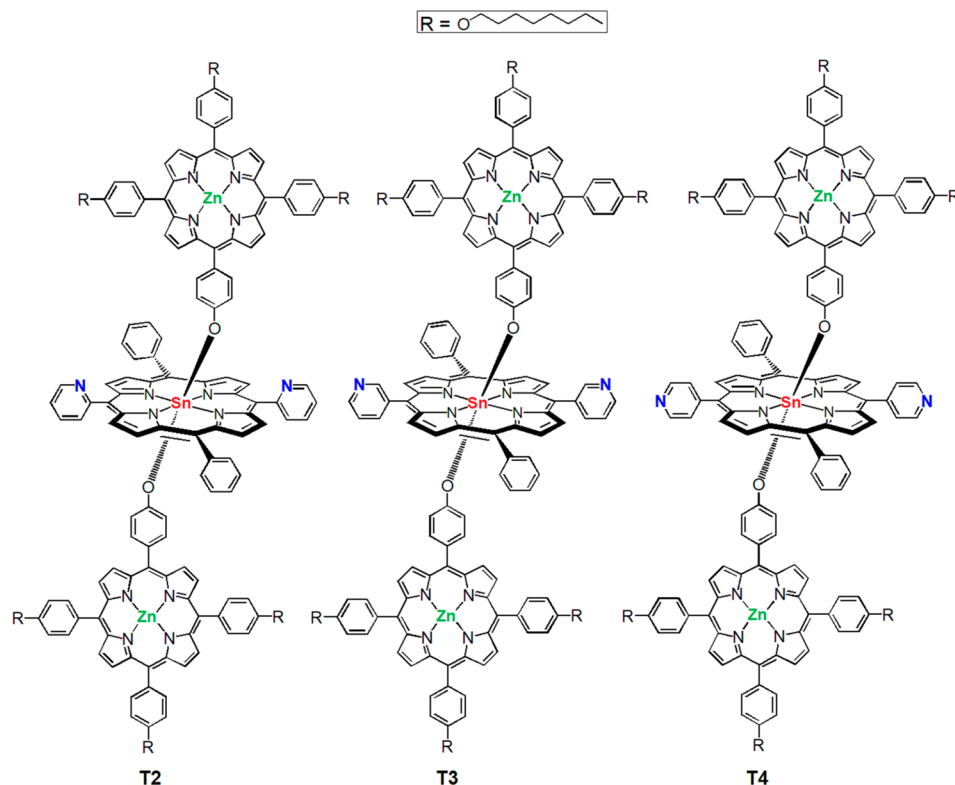
Chart 1. Chemical Structures of Three Isomeric Triads Used in the Present Study

ligand coordination,[42] and surfactant-assisted methods, have been used for the construction of well-defined, discrete self-assembled porphyrin nanoaggregates.[43]

Recently, we have reported several porphyrin-based nanostructures obtained from the reaction between *trans*-dihydroxo-[5,15-bis(3-pyridyl)-10,20-bis(phenyl)porphyrinato] tin(IV) and different Zn(II) porphyrins.[30,31] Intramolecular coordination between the pyridyl nitrogen atom of the Sn(IV) porphyrin and Zn(II) porphyrin, followed by the self-assembly of porphyrin triads, is the main driving force for the formation of these nanostructures. However, studies have been limited to the use of the 3-pyridyl position. Therefore, in this study, we examined the coordination of other pyridyl positions in the Sn(IV) porphyrin to Zn(II) porphyrin. Here, we report three new triad compounds synthesized from the reaction of a Zn(II) porphyrin, **ZnL**, with three different tin(IV) porphyrin precursors. These Sn(IV) porphyrin precursors differ in the *trans*-pyridyl positions (Chart 1). The aim of the present study is to determine the correlation between the coordination mode (pyridyl-*N* of the Sn(IV) porphyrin with the Zn(II) porphyrin) and its effect on the nanomorphology. Our results suggest that the coordination structure affects the morphology of these nanostructures.

In addition, porphyrin-based nanomaterials have tremendous applications in the removal of pollutant dyes from aqueous solutions.[30,31] Water pollution caused by the discharge of highly toxic and hazardous dyes poses a serious threat to the environment and has negative effects on aquatic flora and fauna.[44] Methyl orange (MO) is one of the 20 dyes detected most frequently in wastewater, and it can cause respiratory, skin, and eye irritation. MO is a water-soluble aromatic azo dye (commonly used as a pH indicator) and is extensively used in several industries, including the textile, paper, printing, and food industries. Every year, the textile industry discharges large

quantities of MO into the aqueous ecosystem, resulting in nonpotable water.[45,46] Thus, we also studied the morphology-dependent photocatalytic degradation of MO in aqueous solution by these photocatalysts.

■ EXPERIMENTAL SECTION

Materials and Methods. All chemicals were purchased from Sigma-Aldrich and used without further purification unless otherwise stated. The *trans*-dihydroxo-[5,15-bis(2-pyridyl)-10,20-bis(phenyl)porphyrinato] tin(IV) (**SnP²**), *trans*-dihydroxo-[5,15-bis(3-pyridyl)-10,20-bis(phenyl)porphyrinato] tin(IV) (**SnP³**), and *trans*-dihydroxo-[5,15-bis(4-pyridyl)-10,20- bis(phenyl)porphyrinato] tin(IV) (**SnP⁴**) complexes were synthesized according to a previously reported procedure.[47,30,37] All experiments were carried out under a dry argon atmosphere using standard Schlenk techniques. Toluene was purified by distillation from a sodium/benzophenone ketyl solution, whereas pyrrole was obtained from a solution of calcium hydride. Steady-state UV–vis spectra were recorded on a Shimadzu UV-3600 spectrophotometer. The fluorescence spectra were recorded using a Shimadzu RF-5301PC fluorescence spectrophotometer. The ¹H NMR spectra were obtained on a Bruker BIOSPIN/AVANCE III 400 spectrometer at 293 K, and the electrospray ionization mass spectra (ESI-MS) were recorded on a Thermo Finnigan linear ion trap quadrupole mass spectrometer. Elemental analysis was performed using an EA 1110 Fisons analyzer. Field emission scanning electron microscopy (FE-SEM) images were obtained using a MAIA III SEM device. For sample preparation, each compound was suspended in toluene at a fixed concentration ($c = 0.5$ mM) and centrifuged at 13 500 rpm for 20 s. After that, this solution was drop-cast on the surface of Cu tapes and then dried in air. After deposition and before the FE-SEM measurements, a Pt coating

was applied. The Brunauer—Emmett—Teller (BET) surface area using N_2 adsorption isotherms at 77 K was determined with an analyzer (BELSORP-mini volumetric adsorption equipment). The total organic carbon (TOC) values of the degradation of MO were detected with a JEOL JEM-3010 total organic carbon analyzer to determine the extent of mineralization.

Synthesis of 4-Octoxybenzaldehyde. For the synthesis of 4-octoxybenzaldehyde, we used a previously reported procedure with some modifications.[48] Briefly, a mixture of 4-hydroxybenzaldehyde (8.84 g, 72.4 mmol), K_2CO_3 (14 g, 109 mmol), and KI (1.08 g, 7.24 mmol) was dissolved in dry dimethylformamide (DMF, 50 mL) and stirred at room temperature under an argon atmosphere. Then, 1-bromooctane (14 mL, 72.4 mmol) was added to the above reaction mixture and held at 100 °C for 24 h. The reaction mixture was then filtered, and the filtrate was removed under vacuum. The residue was dissolved in ethyl acetate and washed with water. The organic layer was then dried over anhydrous $MgSO_4$, and the solvent was evaporated under reduced pressure. Pure 4-octoxybenzaldehyde was separated from the crude product by column chromatography (ethyl acetate/n-hexane = 1/10) and dried under vacuum. Yield: 15.2 g (90%). ^{1}H NMR (400 MHz, CDCl$_3$, ppm): δ 0.84 (t, 3H, CH$_3$), 1.15−1.30 (m, 10H, alkyl chain), 1.74 (m, 2H, O−C−CH$_2$), 3.97 (t, 2H, O−CH$_2$), 6.94 (d, J = 8.7 Hz, 2H, H3,5-PhCHO), 7.39 (d, J = 8.7 Hz, 2H, H2,6-PhCHO), 9.81 (s, H, CHO).

Synthesis of meso-5-(4-Hydroxyphenyl)-10,15,20-tris-(4-octoxyphenyl)porphyrin, H$_2$L. The free base porphyrin was synthesized by mixed aldehyde condensation in propionic acid using 1.0 equiv of 4-hydroxybenzaldehyde, 3.0 equiv of 4-substituted benzaldehyde, and 4.0 equiv of pyrrole. In a typical reaction, pyrrole (0.77 mL, 11.1 mmol) was added dropwise to a solution of 4-hydroxybenzaldehyde (0.34 g, 2.8 mmol) and 4-octoxybenzaldehyde (1.97 g, 8.4 mmol) in propionic acid (200 mL) under reflux. The mixture was stirred for 3 h, and then the solvent was evaporated under reduced pressure. The crude product was purified by column chromatography (SiO$_2$, n-hexane/CH$_2$Cl$_2$ eluent) to afford **H$_2$L** and recrystallized from a CH$_2$Cl$_2$/acetonitrile mixture to give a violet−purple powder. Yield: 0.243 g (8%). Anal. Calcd for C$_{73}$H$_{90}$N$_4$O$_4$: C, 80.62; H, 8.34; N, 5.15; R, 5.88. Found: C, 81.21; H, 8.62; N, 4.90; R, 5.27. ^{1}H NMR (400 MHz, CDCl$_3$, ppm): δ −2.79 (s, 2H, NH), 0.92 (t, 9H, CH$_3$), 1.34−1.48 (m, 24H, alkyl chain), 1.63 (m, 6H, O−C−C−CH$_2$), 1.96 (m, 6H, O−C−CH$_2$), 4.22 (t, 6H, O−CH$_2$), 7.16 (d, J = 8.4 Hz, 2H, H2,6-PhOH), 7.30 (d, J = 8.4 Hz, 6H, H2,6-Ar), 8.04−8.08 (m, 8H, meso-O-Ar + meso-O-PhOH), 8.85 (m, 8H, β-pyrrole). UV−visible (CHCl$_3$): λ$_{nm}$ (log ε), 423 (5.31), 522 (4.21), 559 (3.92), 597 (3.87), 649 (3.83). Emission (CHCl$_3$, λ$_{nm}$): 652, 712.

Synthesis of meso-5-(4-Hydroxyphenyl)-10,15,20-tris-(4-octoxyphenyl)porphyrinato)zinc(II), ZnL. Zn(OAc)$_2$·2H$_2$O (0.053 g, 0.29 mmol) was added to a solution of **H$_2$L** (0.122 g, 0.12 mmol) in a mixture of tetrahydrofuran (THF, 15 mL) and methanol (15 mL). The mixture was refluxed for 3 h. The solvent was then removed, and the solid product was purified by column chromatography (SiO$_2$, n-hexane/CH$_2$Cl$_2$ eluent). The crude product was recrystallized from CH$_2$Cl$_2$/acetonitrile to yield a brownish-red color. Yield: 0.113 g (90%). Anal. Calcd for C$_{73}$H$_{88}$N$_4$O$_4$Zn: C, 76.18; H, 7.71; N, 4.87; R, 11.24. Found: C, 76.02; H, 7.93; N, 4.73; R, 11.32. ^{1}H NMR (400 MHz, deuterated dimethyl sulfoxide (DMSO-d_6), ppm): δ 0.92 (t, 9H, CH$_3$), 1.30−1.50 (m, 24H, alkyl chain), 1.56 (m, 6H, O−C−C−CH$_2$), 1.90 (m, 6H, O−C−CH$_2$), 4.24 (t, 6H,

O−CH$_2$), 7.17 (d, J = 8.4 Hz, 2H, H2,6-PhOH), 7.32 (d, J = 8.4 Hz, 6H, H2,6-Ar), 7.96 (d, J = 8.0 Hz, 2H, meso-O-PhOH), 8.05 (d, J = 8.0 Hz, 6H, meso-O-Ar), 8.81 (m, 8H, β-pyrrole), 9.90 (s, 1H, OH). UV−visible (CHCl$_3$): λ$_{nm}$ (log ε), 425 (5.40), 560 (4.03), and 601 (3.78). Emission (CHCl$_3$, λ$_{nm}$): 610, 657.

General Procedure for the Synthesis of the Triads. A mixture of **ZnL** (0.092 g, 0.08 mmol) and **SnP^n** (0.031 g, 0.04 mmol) was added to anhydrous toluene (10 mL) and refluxed for 48 h under an Ar atmosphere. Then, the solvent was removed (for **T2** and **T4**), and the solid compound was purified by neutral silica chromatography (n-hexane/CH$_2$Cl$_2$ eluent). For **T3**, the reaction mixture was cooled to room temperature, and the colored precipitate was filtered out, washed with toluene, and dried under vacuum.

Synthesis of Triad T2. Brick-red compound. Yield: 0.092 g, 80%. Anal. Calcd for C$_{178}$H$_{176}$N$_{14}$O$_8$SnZn$_2$: C, 74.00; H, 6.14; N, 6.76; R, 13.10. Found: C, 73.68; H, 6.27; N, 6.54; R, 13.51. ^{1}H NMR (400 MHz, DMSO-d_6, ppm): δ 0.92 (t, 18H, CH$_3$), 1.24−1.48 (m, 48H, alkyl chain), 1.58 (m, 12H, O−C−C−CH$_2$), 1.88 (m, 12H, O−C−CH$_2$), 2.65 (d, J = 8.6 Hz, 4H, α-bridging phenyl), 4.26 (t, 12H, O−CH$_2$), 6.70 (d, J = 8.8 Hz, 4H, β-bridging phenyl), 7.26 (d, J = 8.4 Hz, 12H, m-phenyl-axial), 7.48 (m, 8H, m,p-phenyl-central + H4-Py-central), 7.70 (m, 14H, meso-O-phenyl-axial + H5-Py-central), 8.09 (m, 6H, H3-Py-central + meso-O-phenyl-central), 8.38 (d, J = 7.8 Hz, 4H, β-pyrrole-axial), 8.55 (d, J = 7.8 Hz, 4H, β-pyrrole-axial), 8.70 (m, 8H, β-pyrrole-axial), 9.08 (d, J = 8.2 Hz, 4H, β-pyrrole-central), 9.18 (d, J = 8.2 Hz, 4H, β-pyrrole-central), 9.32 (d, J = 5.4 Hz, 2H, H6-Py). UV−vis (CHCl$_3$): λ$_{nm}$ (log ε), 422 (5.60), 560 (4.60), and 602 (4.35). Emission (CHCl$_3$, λ$_{nm}$): 598, 644.

Synthesis of Triad T3. Bluish-green compound. Yield: 0.105 g, 91%. Anal. Calcd for C$_{178}$H$_{176}$N$_{14}$O$_8$SnZn$_2$: C, 74.00; H, 6.14; N, 6.76; R, 13.10. Found: C, 73.82; H, 6.47; N, 6.66; R, 13.05. ^{1}H NMR (400 MHz, DMSO-d_6, ppm): δ 0.91 (t, 18H, CH$_3$), 1.20−1.48 (m, 48H, alkyl chain), 1.57 (m, 12H, O−C−C−CH$_2$), 1.90 (m, 12H, O−C−CH$_2$), 2.67 (d, J = 8.6 Hz, 4H, α-bridging phenyl), 4.26 (t, 12H, O−CH$_2$), 6.70 (d, J = 8.8 Hz, 4H, β-bridging phenyl), 7.27 (m, 18H, {m,p-phenyl}-axial), 7.60−7.76 (m, 20H, m,p-phenyl-central + H5-Py-central + meso-O-phenyl-axial), 8.12 (m, 6H, H4-Py-central + meso-O-phenyl-central), 8.42 (d, J = 7.8 Hz, 4H, β-pyrrole-axial), 8.57 (d, J = 7.8 Hz, 4H, β-pyrrole-axial), 8.72 (m, 8H, β-pyrrole-axial), 9.08 (d, J = 8.2 Hz, 4H, β-pyrrole-central), 9.18 (d, J = 8.2 Hz, 4H, β-pyrrole-central), 9.30 (d, J = 5.2 Hz, 2H, H6-Py), 9.55 (s, 2H, H2-Py). UV−visible (CHCl$_3$): λ$_{nm}$ (log ε), 428 (5.49), 453 (5.35), 565 (4.81), 613 (4.78). Emission (CHCl$_3$, λ$_{nm}$): 598, 645.

Synthesis of Triad T4. Dark-red compound. Yield: 0.097 g, 84%. Anal. Calcd for C$_{178}$H$_{176}$N$_{14}$O$_8$SnZn$_2$: C, 74.00; H, 6.14; N, 6.76; R, 13.10. Found: C, 73.49; H, 6.32; N, 6.56; R, 13.65. ^{1}H NMR (400 MHz, DMSO-d_6, ppm):): δ 0.91 (t, 18H, CH$_3$), 1.22−1.48 (m, 48H, alkyl chain), 1.58 (m, 12H, O−C−C−CH$_2$), 1.89 (m, 12H, O−C−CH$_2$), 2.66 (d, J = 8.6 Hz, 4H, α-bridging phenyl), 4.26 (t, 12H, O−CH$_2$), 6.70 (d, J = 8.8 Hz, 4H, β-bridging phenyl), 7.26 (d, J = 8.4 Hz, 12H, m-phenyl-axial), 7.56 (m, 6H, m,p-phenyl-central), 7.72 (d, J = 8.0 Hz, 12H, meso-O-phenyl-axial), 8.14 (m, 8H, H3-Py-central + meso-O-phenyl-central), 8.42 (d, J = 7.8 Hz, 4H, β-pyrrole-axial), 8.58 (d, J = 7.8 Hz, 4H, β-pyrrole-axial), 8.75 (m, 8H, β-pyrrole-axial), 9.09 (m, 8H, β-pyrrole-central), 9.26 (d, J = 5.4 Hz, 4H, H6-Py). UV−visible (CHCl$_3$): λ$_{nm}$ (log ε), 426 (5.53), 448

(5.01), 563 (4.57), 605 (4.43). Emission (CHCl$_3$, λ_{nm}): 598, 646.

Photocatalytic Degradation of Methyl Orange. The photocatalytic activity of the nanostructures was studied by monitoring the degradation of methyl orange (MO) dye in an aqueous medium. In a typical process, 10 mg of the photocatalyst (**T2**, **T3**, or **T4**) was added to 150 mL of an aqueous MO solution (20 mg L^{-1}, pH 7) with stirring. Before visible-light irradiation, the mixture was kept in the dark for 15 min to reach an adsorption–desorption equilibrium. Subsequently, the reaction mixture was exposed to visible light irradiation from a 150 W xenon arc lamp (ABET Technologies, USA) with a UV cutoff filter at room temperature. All sample solutions were collected by centrifugation (to remove the photocatalyst) at given time intervals to determine the MO concentration by UV–vis spectroscopy at 461 nm.

RESULTS AND DISCUSSION

Synthesis and Characterization. For the synthesis of the three isomeric triads in Chart 1, we used the "axial bonding" approach.[30,31,49−52] All of these triads were synthesized by refluxing *meso*-5-(4-hydroxyphenyl)-10,15,20-tris(4-octoxyphenyl)porphyrinato)zinc(II) (**ZnL**) with the corresponding *trans*-dihydroxo Sn(IV) porphyrins **SnP^n** in anhydrous toluene for 48 h under an argon atmosphere (Scheme 1). Complete details of the experiments are given in the Experimental Section. The average yield was found to be more than 70% in all cases. The strong affinity of the aryloxides toward the Sn(IV) porphyrin center was the driving force for the formation of
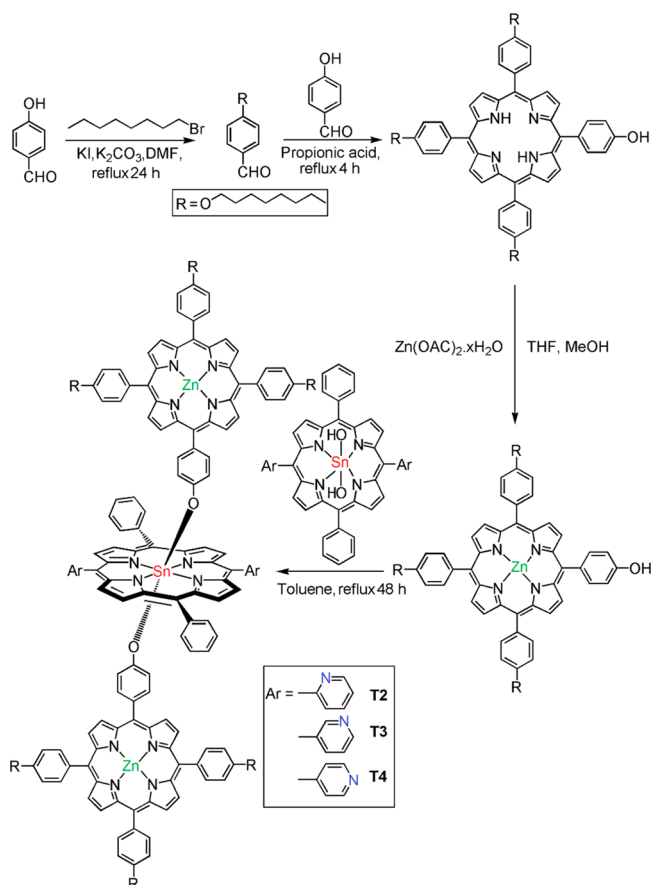
these triads. All of the synthesized compounds were fully characterized by elemental analysis and spectroscopic techniques including ^{1}H NMR spectroscopy, ESI-MS, UV–vis spectroscopy, and fluorescence spectroscopy.

The ^{1}H NMR spectra of all three isomeric triads and the individual unconnected monomers (**H$_2$L** and **ZnL**) are given in the Supporting Information (Figures S1−S5). All of the peaks were assigned, and the peak integrals are given in the Experimental Section. From the ^{1}H NMR spectra of these three triads, it is clear that the resonance positions of the aromatic protons as well as the β-pyrrolic protons of the central Sn(IV) porphyrin are not significantly different from those of the starting Sn(IV) porphyrins (**SnP^n**).

In the ^{1}H NMR spectra, the pyridyl protons of the triads appear as doublets (9.32 ppm for **T2**, 9.30 and 9.55 ppm for **T3**, and 9.26 ppm for **T4**). In contrast, the β-pyrrolic protons of triads **T2** and **T3** appear from 9.08 to 9.18 ppm (doublet), and those for **T3** appear as a doublet at 9.09 ppm. The remaining aromatic protons of the central **SnP^n** unit in the triads appear from 7.5 to 8.15 ppm. On the other hand, the protons of the axial Zn(II) porphyrins in the triads are different from those of the monomeric **ZnL** in terms of the splitting patterns and resonance positions. This is due to the strong ring-current effects of the central Sn(IV) porphyrins on the axial Zn(II) porphyrins. In particular, the aryloxy protons appeared as a doublet at 7.17 and 7.96 ppm in the NMR spectrum of monomeric **ZnL**. In the triads, these two protons experienced strong shielding effects from the ring-current effects of the central Sn(IV) porphyrins, appearing as a doublet at 2.65 and 6.70 ppm. The $\Delta\delta$ values [that is, δ(**ZnL**) − δ(triad)] for these protons are approximately 4.52 and 1.26 ppm, respectively. In addition, the β-pyrrole protons of the axial Zn(II) porphyrin in the triads are exposed to ring-current effects similar to that of monomeric **ZnL**. Specifically, the β-pyrrole protons resonated at 8.81 ppm in monomeric **ZnL**. However, these protons in the triads were shifted upfield and split into three different positions (approximately 8.40, 8.55, and 8.70 ppm). The chemical shifts of the remaining protons associated with the axial Zn(II) porphyrins showed no further changes compared to those of monomeric **ZnL**. ^{1}H NMR measurements have been extensively used to explore "axial-bonding"-type architectures based on the interactions between the protons of axial Zn(II) porphyrins and those of the central Sn(IV) porphyrin involving ring-current-induced shifts and resonance couplings.[30,31,49,50]

The results of ESI-MS measurements of all three triads are shown in the Supporting Information (Figures S6−S8). From Figure S6, it is clear that compound **T2** was fragmented during the MS experiments.[30,31] However, the molecular ion peak [**T2** + H]$^+$ at a mass-to-charge (m/z) ratio of 2889.89 appeared with low intensity. On the other hand, a base peak at 769.13, corresponding to [**SnP^2** + H]$^+$, was observed. Similar MS patterns were observed for the other two triads.

The UV–visible spectra of all three triads in CHCl$_3$ solution, along with that of **ZnL**, are shown in Figure 1. The maximum absorbance (λ_{max}) and molar extinction coefficient (ε) of all of the compounds are reported in the Experimental Section. The monomeric Zn(II) porphyrin (**ZnL**) had a Soret band (at approximately 425 nm) and Q-bands (at approximately 560 and 601 nm). Insignificant changes in the spectrum of **T2** were observed (the Soret band at 422 nm is quite broad) compared to that of **ZnL**. Furthermore, the molar extinction coefficient of **T2** is very close to the sum of those of the monomeric Sn(IV) porphyrin and **ZnL**. In contrast, the spectral features of **T3** and
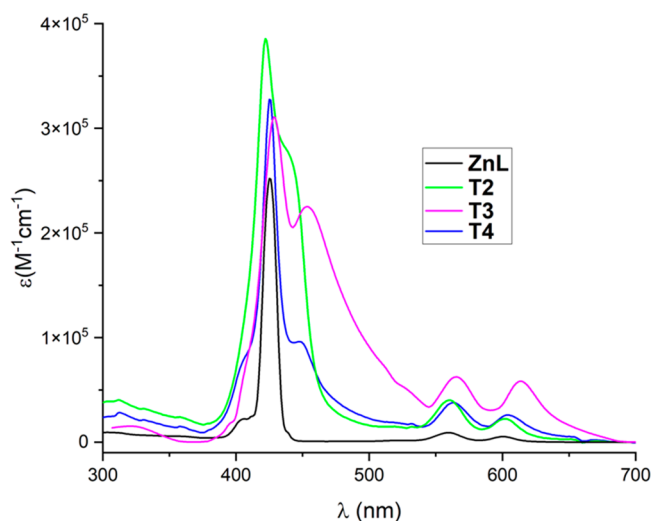
Scheme 1. Synthesis Scheme Used to Prepare the Triads

Figure 1. UV−visible spectra of the three triads and **ZnL** in CHCl$_3$.

Figure 2. Fluorescence spectra of all three triads and **ZnL** in CHCl$_3$ (λ_{ext} = 550 nm). The optical density (OD) of each sample solution was fixed at 0.25.

Figure 3. FE-SEM images showing the morphologies of (a) **ZnL**, (b) **T2**, (c) **T3**, and (d) **T4**.

T4 were different from those of **T2**. The spectrum of **T3** is broad in the Soret region with a small red shift (approximately 428 nm) along with the Q-bands (approximately 565 and 613 nm) compared to those of **ZnL**. Additionally, a peak at approximately 453 nm was also found for **T3**. In the case of **T4**, the Soret band is present at approximately 426 nm, and the Q-bands are present at approximately 563 and 605 nm, along with a small peak at 448 nm.

The ground-state data indicate that there are minimal perturbations to the electronic structures of the individual macrocyclic π-systems in these triads. In addition, axial−axial, basal−basal, or axial−basal couplings between the axial Zn(II) porphyrin and basal Sn(IV) porphyrin rings were not observed.[30,31,49,50] Therefore, the red shift in the peak position (λ_{max}) and the peak broadening of the Soret bands indicate that a *J*-type or step-like self-assembled arrangement is possible in solution.[30,31,53]

Steady-state fluorescence spectra of all three triads, along with those of **ZnL**, were recorded in CHCl$_3$ and are shown in Figure 2. **ZnL** yielded two-banded fluorescence spectra having emission maxima at 610 and 657 nm. In contrast, all of the triads showed similar two-banded spectra having emission maxima at 598 and 645 nm. The peak-to-peak intensity ratio also decreased from **ZnL** to these triads. As shown in Figure 2, the emissions of all these triads were quenched, and the degree of quenching was significantly affected by their aggregation in solution.[30,31]

Supramolecular Self-Aggregation. The morphology and self-assembly behavior of all of the compounds were analyzed using FE-SEM. The FE-SEM images are shown in Figure 3. Figure 3a shows that **ZnL** has a nanostructured morphology, but the particle shape and size are very irregular. In contrast, nanospheres of different sizes were observed for **T2** (Figure 3b), and the average diameter of the smaller nanospheres ranged from 60 to 80 to nm, whereas the average diameter of the larger nanospheres varied from to 220 to 240 nm. Well-defined nanorods were observed for **T3** (Figure 3c), the average length of the nanorods varied from 160 to 900 nm, the average width of the nanorods ranged from 40 to 90 nm, and the height of the nanorods was approximately 20 nm. On the other hand, variably shaped nanoaggregates were observed for **T4** (Figure 3d) and comprised small particles, along with some long nanoflakes with interconnected smaller particles. The average lengths of the
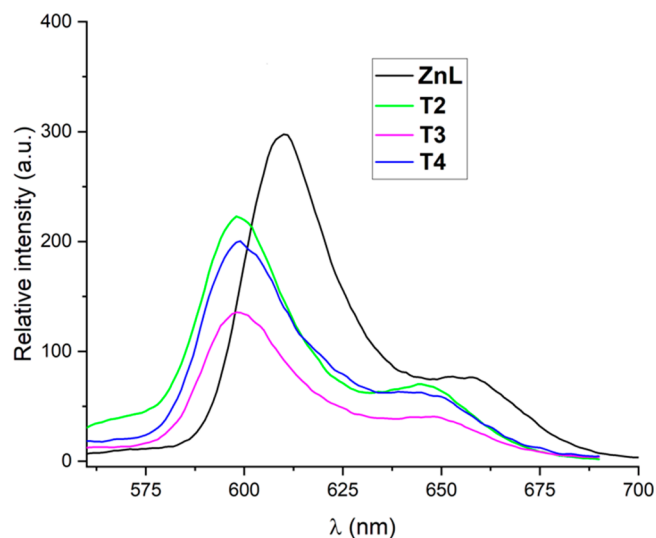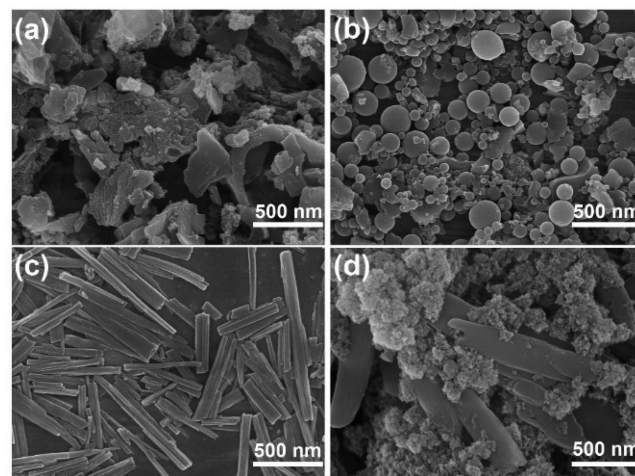
nanoflakes varied from 800 to 1200 nm. The average width of the nanoflakes varied from 200 to 260 nm.

From the FE-SEM images in Figure 3, it is clear that all of the compounds formed nanoscale aggregates. Typically, porphyrin (free-base porphyrin or metalated porphyrin) molecules are aggregated into nanostructures via self-assembly. Here, monomeric Zn(II) porphyrins are self-assembled via π−π stacking interactions between adjacent porphyrin molecules and form nanostructures. Similarly, **T2** aggregated to form spherical particles as well. In contrast, the morphology of **T3** was quite different: nanorods with well-defined shapes and sizes. The pyridyl groups in **T3** coordinate intramolecularly to the Zn ion in the axial Zn(II) porphyrin, thus locking the axial porphyrin units into position, which facilitates self-assembly via π−π stacking interactions through face-to-face interactions.[30,31] In contrast, for **T4**, the coordination of the pyridyl-*N* to the axial Zn(II) porphyrins occurs in an intermolecular manner. Therefore, intermolecular coordination and π−π stacking interactions drive the aggregation of **T4**. A similar coordination mode is not possible in **T2** because of the geometrical

constraints within the molecule. It should be noted that the other starting porphyrin monomers, **SnP^n**, did not show any aggregation under our experimental conditions.[30,31]

Photocatalytic Degradation of Methyl Orange (MO). The photocatalytic degradation of MO in aqueous solution was used to evaluate the photocatalytic activity of the three triads under visible light irradiation, and the results are shown in Figure 4. For comparison, the photocatalytic performance of
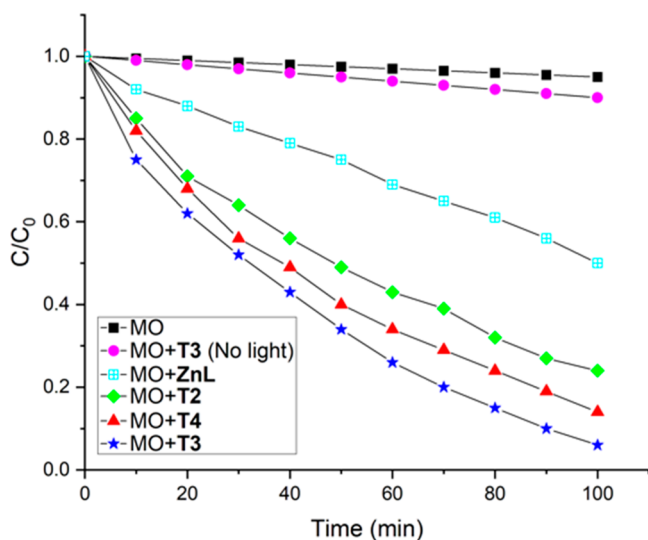

Figure 4. Photocatalytic degradation of MO in aqueous solution (pH 7, 298 K) under visible-light irradiation.

monomeric **ZnL** was also measured. The degradation of MO dye in the presence of monomeric **SnP^n** was not measured. A low degree of dye degradation was observed in the absence of both visible light and a photocatalyst (Figure 4). Therefore, both visible light irradiation and a photocatalyst are required to degrade MO. Time-dependent measurements of the absorption spectra of MO in aqueous solution in the presence of the **T3** nanorods under visible light irradiation are shown in Figure S9. The degradation of MO dye was monitored by measuring the decay of the absorbance peak at 461 nm with respect to irradiation time. The photocatalytic efficiency of the different nanomaterials for the degradation of MO is expressed using the degradation efficiency, $(C_0-C)/C_0$, where C_0 is the initial concentration of MO and C is the concentration at time t. As shown in Figure 4, of the photocatalysts, **T3** exhibited the best efficiency for the degradation of MO within 100 min of visible-light irradiation, and the observed degradation ratios reached 94, 86, 76, and 50% for **T3**, **T4**, **T2**, and **ZnL**, respectively. These results suggest that the efficiency of the photocatalytic degradation of MO is affected by the photocatalyst morphology. In general, different morphologies can affect the catalytic activity because they provide different sizes, surface areas, numbers of active sites, and numbers of defects. Especially for **T3**, the one-dimensional rodlike shape probably promotes the electron-transfer process, providing more efficient photocatalytic performance. Similarly, the nanofibers of ZnTPyP (*meso*-tetra(4-pyridyl)porphyrinato)Zn(II) exhibited distinct photocatalytic performance for the photodegradation of rhodamine B (RhB) molecules compared to the nanosphere, and it was revealed that the formation of *J*-aggregates in the nanofibers facilitates the electron-transfer process, resulting in distinct photocatalytic performance.[54] In addition, the ZnTPyP nano-

wire showed enhanced photocatalytic performance for the MO degradation and H$_2$ production compared to other morphologies such as nanospheres and nanooctahedra.[55] On the other hand, the surface area of the catalyst had little influence on the performance. Each catalyst exhibited a low surface area, for example, the BET surface area of the best-performing **T3** was measured to be 30 m^2/g by using N$_2$ adsorption isotherms at 77 K (Figure S10). For comparison, commercial TiO$_2$ (anatase) and ZnO nanoparticles have surface areas of approximately 186 and 88 m^2/g, respectively.

The reaction kinetics for the decomposition of MO were also investigated. For this, we used the pseudo-first-order model as expressed by $\ln(C_0/C) = kt$, which is commonly used for photocatalytic degradation experiments if the initial concentration of the pollutant or dye is low. In this equation, k is the pseudo-first-order rate constant. Using the data in Figure 4, we plotted $\ln(C_0/C)$ versus t and obtained the rates of MO decomposition by these photocatalysts (Figure S11). The first-order rate constant for the degradation of MO by **T3** (0.0251 min^{-1}) is higher than those of **T4** (0.018 min^{-1}), **T2** (0.015 min^{-1}), and **ZnL** (0.006 min^{-1}). Notably, these rates are comparable to or even better than those previously reported for inorganic photocatalysts such as Ag$_2$O (0.007 min^{-1}),[56] ZnO (0.005 min^{-1}),[57] and TiO$_2$ (0.015 min^{-1}).[58]

Consecutive degradation reactions were conducted to verify the stability of the photocatalysts in aqueous solution. The catalysts were separated by centrifugation after each reaction, washed twice with distilled water, and dried under vacuum (323 K). Subsequently, the catalysts were used for repeated dye-degradation cycles. Importantly, the photocatalyst efficiency remained intact even after 10 consecutive cycles. As depicted in Figure 5, 94% MO was degraded within 100 min for the first run, and the photocatalytic performance decreased slightly, marked by 90% MO degradation, after 10 consecutive cycles. The high stability of **T3** was confirmed by FE-SEM. No significant change
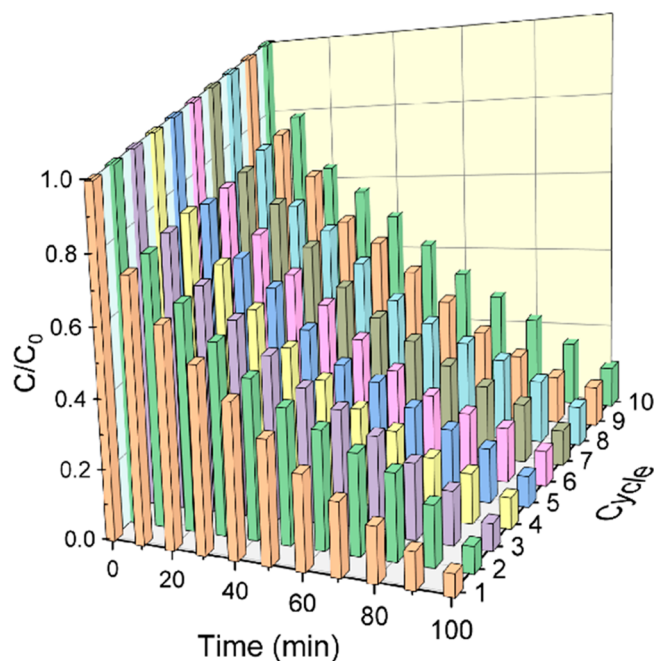

Figure 5. Consecutive cycling photodegradation curves of MO with **T3** in aqueous solution.

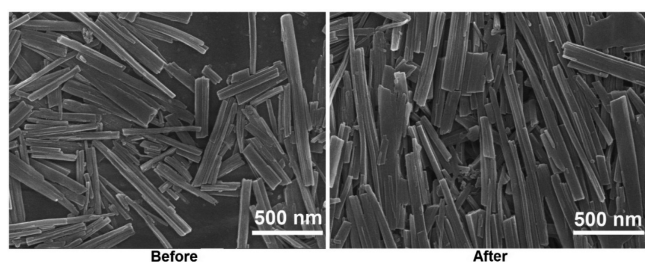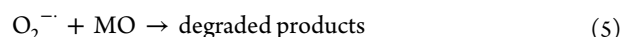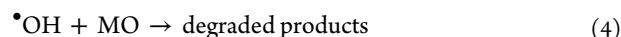was observed in the morphology of **T3** after 10 cycles as shown in Figure 6.

Figure 6. FE-SEM images of **T3** before and after 10 consecutive cycles.

Next, we optimized the photocatalyst/MO ratio during the degradation experiments. For this purpose, different concentrations of MO (5, 10, 15, and 20 mg L^{-1}) with a constant amount of photocatalyst (10 mg) were used at 298 K and pH 7. It was found that 20 mg L^{-1} of MO dye solution (150 mL) with 10 mg of photocatalyst yielded the best performance (Figure S12). We further examined the influence of pH on the photocatalytic degradation of MO dye. In Figure S13, it can be seen that the degradation performance is comparable to over 80% in the range of pH 5−9. However, the performance declined significantly under highly acidic or basic conditions. Inhibited coordination bonding under these harsh conditions can cause the nanostructures to collapse, thus degrading the performance.

Several possible mechanisms for the photodegradation of pollutant dyes in aqueous solutions using similar photocatalysts have been reported.[30,31] When a photocatalyst is subjected to visible-light irradiation in the presence of MO, the nanomaterial absorbs light, and the valence band (VB) electrons are promoted to the conduction band (CB) across the band gap. This causes the formation of electron−hole pairs (e^-/h^+) pairs at the surface of the photocatalyst. Strong intermolecular π−π interactions intensify the electron delocalization over the nanoaggregates and minimize the recombination energy of the excited electrons. Then, the photogenerated holes (h^+) react with H_2O to produce hydroxyl radicals ($^\bullet OH$), and the electrons react with the dissolved O_2 to produce superoxide radical anions ($O_2^{-\bullet}$). These highly reactive photogenerated superoxide radical anions and hydroxyl radicals react with MO, resulting in its degradation.

The mechanism consists of several steps for the porphyrin triad (**T**), as shown in eqs 1−5.

$$T + h\nu \rightarrow T^*(e^- + h^+) \tag{1}$$

$$H_2O + h^+ \rightarrow {}^\bullet OH + H^+ \tag{2}$$

$$O_2 + 2e^- \rightarrow O_2^{-\cdot} \tag{3}$$

$${}^\bullet OH + MO \rightarrow \text{degraded products} \tag{4}$$

$$O_2^{-\cdot} + MO \rightarrow \text{degraded products} \tag{5}$$

The reactive species involved in the photocatalytic reactions in the presence of **T3** were revealed by radical trapping analysis.[59] As shown in Figure S14, *para*-benzoquinone (BQ)
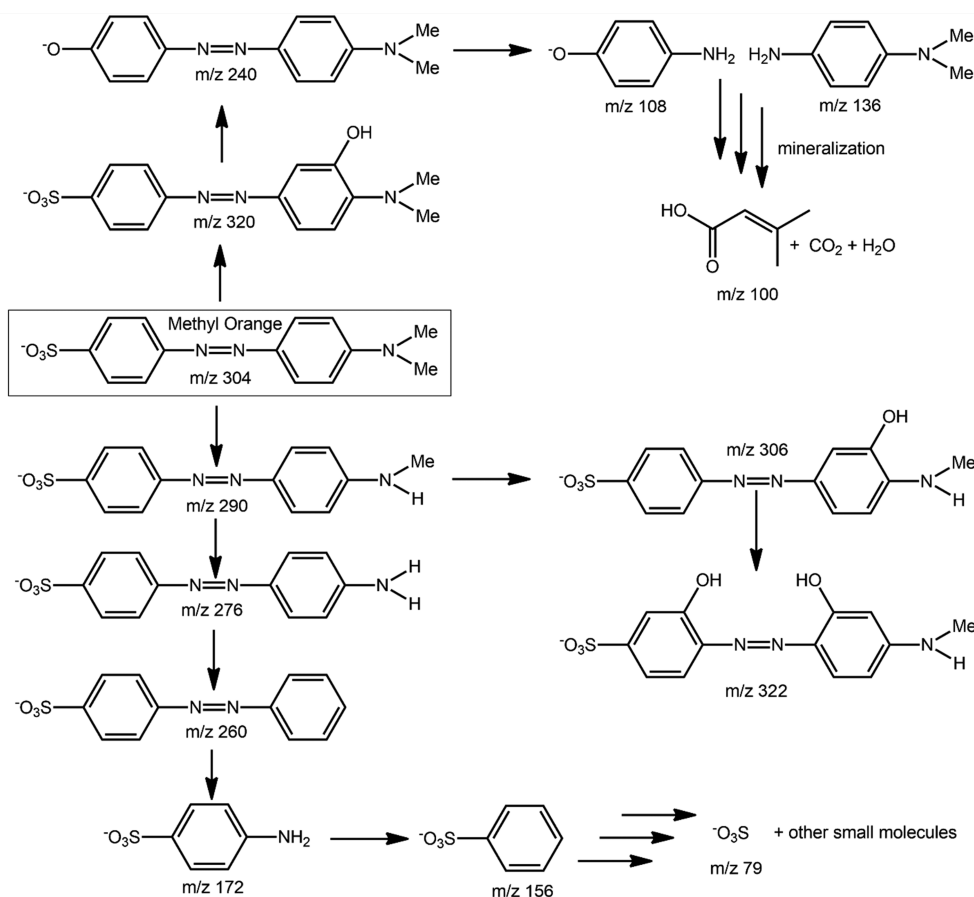

Figure 7. Possible intermediates of the reaction between MO and **T3** under visible-light irradiation in aqueous solution.

and *tert*-butyl alcohol (^{t}BuOH) were used to capture superoxide radical anions ($O_2^{-\bullet}$) and hydroxyl radicals ($^\bullet OH$), respectively, to investigate the effect of different reactive species on the photocatalytic degradation of MO by **T3**. The results show that the MO degradation rate in the presence of **T3** is affected by both ^{t}BuOH and BQ, suggesting that hydroxyl and superoxide radicals are the major reactive species contributing to the catalytic oxidation of MO. For further details on the detection of all intermediate species (singlet or triplet oxygen species, hydroxyl radicals, or superoxide radical anions), readers are directed to our previous reports.[30,31]

To obtain details of the degradation products of MO after photocatalysis, we analyzed the reaction mixture obtained after 1 h by ESI-MS (Figure S15). Compared to the MS pattern of MO, that of the degraded mixture suggests that MO was degraded by visible light photocatalysis.[60] As suggested by the data in Figure S15, three different degradation mechanisms can be proposed. First, the successive demethylation and addition of hydroxyl groups to MO leads to the formation of two intermediates with m/z values of 290 and 320. Second, the cleavage of the azo double bond leads to the generation of intermediates having m/z values of 156 and 172. Finally, the breakdown of the sulfonate group from the ring leads to the formation of intermediates with an m/z value of 79. Other possible intermediates having m/z values of 100, 108, 136, 240, 260, 276, 306, and 322 are also shown in Figure 7. The formed intermediates were further fragmented into small molecules and finally mineralized into CO_2 and H_2O. Additionally, the total organic carbon (TOC) value was measured to evaluate the removal of MO dye by photocatalysts.[61] The TOC removal percentage achieved using **T3** was only 77%.

CONCLUSIONS

Three isomeric Zn(II)−Sn(IV)−Zn(II) porphyrin triads were synthesized from the reaction of **ZnL** with different pyridyl-*N*-containing **SnPⁿ** complexes. The intramolecular cooperative metal−ligand coordination of the 3-pyridyl nitrogen in **SnP³** with axial **ZnL**, followed by the $\pi-\pi$ interactions between adjacent porphyrin triads, is the determining factor affecting the nanomorphology of **T3**. Owing to geometrical constraints, this type of interaction is not possible for **T2**, for which only $\pi-\pi$ interactions affect the self-assembly process. In contrast, in the case of **T4**, intermolecular interactions and $\pi-\pi$ interactions are responsible for the nanostructure. Moreover, the morphology-dependent photocatalytic degradation of MO dye under visible light irradiation was observed for these photocatalysts, and nanorod-shaped **T3** performed better than nanosphere **T2** and nanoflake **T4**. We consequently demonstrated that tuning the coordination mode enabled us to develop nanostructured photocatalysts with high efficiency for the degradation of MO. Several metal oxides (Ag_2O,[56] ZnO,[57] and TiO_2[58]), a bismuth-based photocatalyst,[62] and a graphitic carbon nitride (g-C_3N_4)-based photocatalyst[63] have been used in advanced oxidation processes (AOPs) for the degradation of pollutant dyes. In particular, TiO_2 has been used as a common photocatalyst because of its low cost, high stability, low toxicity, and high catalytic efficiency toward the degradation of organic pollutants in water, but its large band gap (~3.2 eV) limits the utilization of sunlight owing to the low photocatalytic efficiency in the visible region. Our strategy is much more expandable in the development of visible-light-active photocatalysts because the morphology-controlled fabrication can be readily achieved by molecular engineering. Therefore, precisely engineered por-

phyrin-based materials could be an alternative to the photocatalysts for the treatment of dye-containing wastewater in the near future.

ASSOCIATED CONTENT

Ⓢ Supporting Information

The Supporting Information is available free of charge at https://pubs.acs.org/doi/10.1021/acsomega.2c00022.

> ${}^1H$ NMR spectra, mass spectra, and results for the photocatalytic degradation of MO; ${}^1H$ NMR spectra of **H₂L**, **ZnL**, **T2**, **T3**, and **T4**; ESI-MS spectra of **T2**, **T3**, and **T4**; absorption spectra of MO in the presence of **T3**; adsorption and desorption isotherms of N_2 for **T3** at 77 K; kinetics of the photocatalytic degradation of MO; concentration effect of MO dye solution upon photodegradation by **T3** (10 mg) within 100 min of visible-light irradiation; pH effect of MO dye solution on the photodegradation by **T3**; photocatalytic degradation of MO by the addition of different scavengers; and ESI-MS spectrum of the reaction mixture of MO from the photocatalytic degradation by **T3** (PDF)

AUTHOR INFORMATION

Corresponding Author

Hee-Joon Kim − *Department of Applied Chemistry, Kumoh National Institute of Technology, Gumi 39177, Republic of Korea;* ⓞ orcid.org/0000-0002-2821-6052; Email: hjk@kumoh.ac.kr

Author

Nirmal Kumar Shee − *Department of Applied Chemistry, Kumoh National Institute of Technology, Gumi 39177, Republic of Korea*

Complete contact information is available at:
https://pubs.acs.org/10.1021/acsomega.2c00022

Author Contributions

N.K.S. is responsible for the investigation, methodology, data curation, visualization, formal analysis, validation, software, and writing. H.-J.K. is responsible for the conceptualization, review, editing, supervision, project administration, and funding acquisition.

Notes

The authors declare no competing financial interest.

ACKNOWLEDGMENTS

REFERENCES

(1) Zhang, Q.; Uchaker, E.; Candelaria, S. L.; Cao, G. Nanomaterials for Energy Conversion and Storage. *Chem. Soc. Rev.* **2013**, *42*, 3127−3171.

(2) Astruc, D. Introduction: Nanoparticles in Catalysis. *Chem. Rev.* **2020**, *120*, 461−463.

(3) Munonde, T. S.; Nomngongo, P. N. Nanocomposites for Electrochemical Sensors and Their Applications on the Detection of Trace Metals in Environmental Water Samples. *Sensors* **2021**, *21*, 131.

(4) Ariga, K.; Ito, H.; Hill, J. P.; Tsukube, H. Molecular recognition: from solution science to nano/materials technology. *Chem. Soc. Rev.* **2012**, *41*, 5800−5835.

(5) McNamara, K.; Tofail, S. A. M. Nanoparticles in Biomedical Applications. *Adv. Phys. X* **2017**, *2*, 54−88.

(6) O'Regan, B.; Grätzel, M. A low-cost, high-efficiency solar cell based on dye-sensitized colloidal TiO₂ films. *Nature* **1991**, *353*, 737−740.

(7) Borisova, D.; Möhwald, H.; Shchukin, D. G. Mesoporous silica nanoparticles for active corrosion protection. *ACS Nano* **2011**, *5*, 1939−1946.

(8) Minea, A. A. A review on electrical conductivity of nanoparticle-enhanced fluids. *Nanomaterials* **2019**, *9*, 1592.

(9) Wang, J.; Mu, X.; Sun, M.; Mu, T. Optoelectronic properties and applications of graphene-based hybrid nanomaterials and van der Waals hetero structures. *Appl. Mater. Today* **2019**, *16*, 1−20.

(10) Sadovnikov, S. I.; Vovkotrub, E. G. Thermal stability of nanoparticle size and phase composition of nanostructured Ag₂S silver sulfide. *J. Alloy. Compd.* **2018**, *766*, 140−148.

(11) Wang, S.-P.; Lin, W.; Wang, X.; Cen, T.-Y.; Xie, H.; Huang, J.; Zhu, B.-Y.; Zhang, Z.; Song, A.; Hao, J.; Wu, J.; Li, S. Controllable hierarchical self-assembly of porphyrin-derived supra-amphiphiles. *Nat. Commun.* **2019**, *10*, 1399−1411.

(12) Király, N.; Zeleňák, V.; Lenártová, N.; Zeleňáková, A.; Čižmár, E.; Almáši, M.; Meynen, V.; Hovan, A.; Gyepes, R. Novel Lanthanide-(III) Porphyrin-Based Metal−Organic Frameworks: Structure, Gas Adsorption, and Magnetic Properties. *ACS Omega* **2021**, *6*, 24637−24649.

(13) Shee, N. K.; Seo, J.-W.; Kim, H.-J. Spectrophotometric Study of Bridging *N*-Donor Ligand-Induced Supramolecular Assembly of Conjugated Zn-Trisporphyrin with a Triphenylamine Core. *Molecules* **2021**, *26*, 4771.

(14) Baig, N.; Kammakakam, I.; Falath, W. Nanomaterials: A review of synthesis methods, properties, recent progress, and challenges. *Mater. Adv.* **2021**, *2*, 1821−1871.

(15) Gong, X.; Milic, T.; Xu, C.; Batteas, J. D.; Drain, C. M. Preparation and Characterization of Porphyrin Nanoparticles. *J. Am. Chem. Soc.* **2002**, *124*, 14290−14291.

(16) Drain, C. M.; Varotto, A.; Radivojevic, I. Self-Organized Porphyrinic Materials. *Chem. Rev.* **2009**, *109*, 1630−1658.

(17) Leishman, C. W.; McHale, J. L. Light-Harvesting Properties and Morphology of Porphyrin Nanostructures Depend on Ionic Species Inducing Aggregation. *J. Phys. Chem. C* **2015**, *119*, 28167−28181.

(18) Hasobe, T. Photo- and electro-functional self-assembled architectures of porphyrins. *Phys. Chem. Chem. Phys.* **2012**, *14*, 15975−15987.

(19) Lehn, J.-M. Perspectives in Supramolecular Chemistry—From Molecular Recognition towards Molecular Information Processing and Self-Organization. *Angew. Chem., Int. Ed. Engl.* **1990**, *29*, 1304−1319.

(20) Lee, S. J.; Malliakas, C. D.; Kanatzidis, M. G.; Hupp, J. T.; Nguyen, S. T. Amphiphilic porphyrin nanocrystals: Morphology tuning and hierarchical assembly. *Adv. Mater.* **2008**, *20*, 3543−3549.

(21) Beletskaya, I.; Tyurin, V. S.; Tsivadze, A. Y.; Guilard, R.; Stern, C. Supramolecular chemistry of metalloporphyrins. *Chem. Rev.* **2009**, *109*, 1659−1713.

(22) Durot, S.; Taesch, J.; Heitz, V. Multiporphyrinic Cages: Architectures and Functions. *Chem. Rev.* **2014**, *114*, 8542−8578.

(23) Shao, S.; Rajendiran, V.; Lovell, J. F. Metalloporphyrin nanoparticles: Coordinating diverse theranostic functions. *Coord. Chem. Rev.* **2019**, *379*, 99−120.

(24) Jang, J. H.; Jeon, K.-S.; Oh, S.; Kim, H.-J.; Asahi, T.; Masuhara, H.; Yoon, M. Synthesis of Sn-Porphyrin-Intercalated Trititanate Nanofibers: Optoelectronic Properties and Photocatalytic Activities. *Chem. Mater.* **2007**, *19*, 1984−1991.

(25) Koposova, E. A.; Offenhäusser, A.; Ermolenko, Y. E.; Mourzina, Y. G. Photoresponsive Porphyrin Nanotubes of *Meso*-tetra(4-Sulfonatophenyl)Porphyrin and Sn(IV) *meso*-tetra(4-pyridyl)-porphyrin. *Front. Chem.* **2019**, *7*, 351.

(26) Zargari, S.; Rahimi, R.; Yousefi, A. An efficient visible light photocatalyst based on tin porphyrin intercalated between TiO₂−graphene nanosheets for inactivation of E. coli and investigation of charge transfer mechanism. *RSC Adv.* **2016**, *6*, 24218−24228.

(27) Rahimi, R.; Yaghoubi-Berijani, M.; Zargari, S.; Rabbani, M.; Shariatinia, S. SnTCPP-modified ZnO nanorods prepared via a simple co-precipitation method: application as a new photocatalyst for photodegradation and photoreduction processes. *Res. Chem. Intermed.* **2016**, *42*, 4697−4714.

(28) Tian, Y.; Busani, T.; Uyeda, G. H.; Martin, K. E.; van Swol, F.; Medforth, C. J.; Montan, G. A.; Shelnutt, J. A. Hierarchical cooperative binary ionic porphyrin nanocomposites. *Chem. Commun.* **2012**, *48*, 4863−4865.

(29) Li, C.; Park, K.-M.; Kim, H.-J. Ionic assembled hybrid nanoparticle consisting of tin(IV) porphyrin cations and polyoxomolybdate anions, and photocatalytic hydrogen production by its visible light sensitization. *Inorg. Chem. Commun.* **2015**, *60*, 8−11.

(30) Shee, N. K.; Kim, M. K.; Kim, H.-J. Supramolecular Porphyrin Nanostructures Based on Coordination-Driven Self-Assembly and Their Visible Light Catalytic Degradation of Methylene Blue Dye. *Nanomaterials* **2020**, *10*, 2314.

(31) Shee, N. K.; Kim, H.-J. Self-Assembled Nanomaterials Based on Complementary Sn(IV) and Zn(II)-Porphyrins, and Their Photocatalytic Degradation for Rhodamine B Dye. *Molecules* **2021**, *26*, 3598.

(32) Kim, H. J.; Park, K.-M.; Ahn, T. K.; Kim, S. K.; Kim, K. S.; Kim, D.; Kim, H.-J. Novel fullerene−porphyrin−fullerene triad linked by metal axial coordination: Synthesis, X-ray crystal structure, and spectroscopic characterizations of *trans*-bis([60]fullerenoacetato)tin-(iv) porphyrin. *Chem. Commun.* **2004**, 2594−2595.

(33) Kim, H.-J.; Jo, H. J.; Kim, J.; Kim, S.-Y.; Kim, D.; Kim, K. Supramolecular self-assembly of tin(IV) porphyrin channels stabilizing single-file chains of water molecules. *CrystEngComm* **2005**, *7*, 417−420.

(34) Shee, N. K.; Kim, M. K.; Kim, H.-J. Fluorescent chemosensing for aromatic compounds by supramolecular complex composed of tin(IV) porphyrin, viologen, and cucurbit[8]uril. *Chem. Commun.* **2019**, *55*, 10575−10578.

(35) Kim, M. K.; Shee, N. K.; Lee, J.; Yoon, M.; Kim, H.-J. Photoinduced Electron Transfer upon Supramolecular Complexation of (Porphyrinato)Sn-Viologen with Cucurbit [7] uril. *Photochem. Photobiol. Sci.* **2019**, *18*, 1996−2002.

(36) Kim, H. J.; Shee, N. K.; Park, K. M.; Kim, H.-J. Assembly and X-ray crystal structures of heterometallic multiporphyrins with complementary coordination between ruthenium (II) and tin (IV) porphyrins. *Inorg. Chim. Acta* **2019**, *488*, 1−7.

(37) Shee, N. K.; Lee, C.-J.; Kim, H.-J. Crystal structure of bis (benzoato-κO)[5,15-di-phenyl-10,20-bis(pyridin-4-yl)porphyrinato-κ⁴N,N′,N″,N‴]tin(IV). *IUCrData* **2019**, *4*, x190787.

(38) Shee, N. K.; Lee, C.-J.; Kim, H.-J. Hexacoordinated Sn(IV) porphyrin-based square-grid frameworks exhibiting selective uptake of CO₂ over N₂. *Bull. Korean Chem. Soc.* **2022**, *43*, 103−109.

(39) Fang, H.; Wang, M.; Yi, H.; Zhang, Y.; Li, X.; Yan, F.; Zhang, L. Electrostatic Assembly of Porphyrin-Functionalized Porous Membrane toward Biomimetic Photocatalytic Degradation Dyes. *ACS Omega* **2020**, *5*, 8707−8720.

(40) Wang, Z.; Li, Z.; Medforth, C. J.; Shelnutt, J. A. Self-assembly and self-metallization of porphyrin nanosheets. *J. Am. Chem. Soc.* **2007**, *129*, 2440−2441.

(41) Hasobe, T.; Oki, H.; Sandanayakaa, A. S. D.; Murata, H. Sonication-assisted supramolecular nanorods of meso-diaryl-substituted porphyrins. *Chem. Commun.* **2008**, 724−726.

(42) Maeda, H.; Hasegawa, M.; Hashimoto, T.; Kakimoto, T.; Nishio, S.; Nakanishi, T. Nanoscale Spherical Architectures Fabricated by Metal Coordination of Multiple Dipyrrin Moieties. *J. Am. Chem. Soc.* **2006**, *128*, 10024−10025.

(43) Zhang, C.; Chen, P.; Dong, H.; Zhen, Y.; Liu, M.; Hu, W. Porphyrin Supramolecular 1D Structures via Surfactant-Assisted Self-Assembly. *Adv. Mater.* **2015**, *27*, 5379−5387.

(44) Schwarzenbach, R. P.; Egli, T.; Hofstetter, T. B.; von Gunten, U.; Wehrli, B. Global Water Pollution and Human Health. *Annu. Rev. Environ. Resour.* **2010**, *35*, 109−136.

(45) Zhou, X.-T.; Ji, H.-B.; Huang, X.-J. Photocatalytic Degradation of Methyl Orange over Metalloporphyrins Supported on TiO₂ Degussa P25. *Molecules* **2012**, *17*, 1149−1158.

(46) Castro, K. A. D. F.; Rodrigues, J. M. M.; Faustino, M. A. F.; Tomé, J. P. C.; Cavaleiro, J. A. S.; Neves, M. d. G. P. M. S.; Simões, M. M. Q. Photocatalytic degradation of methyl orange mediated by a silica coated nanomagnet porphyrin hybrid. *J. Organomet. Chem.* **2021**, *938*, 121751.

(47) Bhosale, S. V.; Chong, C.; Forsyth, C.; Langford, S. J.; Woodward, C. P. Investigations of rotamers in diaxial Sn(IV)porphyrin phenolates-towards a molecular timepiece. *Tetrahedron* **2008**, *64*, 8394−8401.

(48) Gong, W.-L.; Xiong, Z.-J.; Li, C.; Zhu, M.-Q. Design, synthesis and photoswitching of broad-spectrum fluorescent hexaarylbiimidazoles. *RSC Adv.* **2014**, *4*, 64371−64378.

(49) Giribabu, L.; Rao, T. A.; Maiya, B. G. Axial-Bonding"-type hybrid porphyrin arrays: Synthesis, spectroscopy, electrochemistry, and singlet state properties. *Inorg. Chem.* **1999**, *38*, 4971−4980.

(50) Kumar, A. A.; Giribabu, L.; Reddy, D. R.; Maiya, B. G. New molecular arrays based on a Tin(IV) porphyrin scaffold. *Inorg. Chem.* **2001**, *40*, 6757−6766.

(51) Shetti, V. S.; Ravikanth, M. Sn(IV) Porphyrin based axial-bonding type porphyrin triads containing heteroporphyrins as axial ligands. *Inorg. Chem.* **2010**, *49*, 2692−2700.

(52) Shetti, V. S.; Ravikanth, M. Supramolecular tetrads containing Sn(IV) porphyrin, Ru(II) porphyrin, and expanded porphyrins assembled using complementary metal−ligand interactions. *Inorg. Chem.* **2011**, *50*, 1713−1722.

(53) Mabesoone, M. F. J.; Markvoort, A. J.; Banno, M.; Yamaguchi, T.; Helmich, F.; Naito, Y.; Yashima, E.; Palmans, A. R. A.; Meijer, E. W. Competing Interactions in Hierarchical Porphyrin Self-Assembly Introduce Robustness in Pathway Complexity. *J. Am. Chem. Soc.* **2018**, *140*, 7810−7819.

(54) Guo, P.; Chen, P.; Ma, W.; Liu, M. Morphology-Dependent Supramolecular Photocatalytic Performance of Porphyrin Nano-assemblies: From Molecule to Artificial Supramolecular Nanoantenna. *J. Mater. Chem.* **2012**, *22*, 20243−20249.

(55) Wang, J.; Zhong, Y.; Wang, L.; Zhang, N.; Cao, R.; Bian, K.; Alarid, L.; Haddad, R. E.; Bai, F.; Fan, H. Morphology-Controlled Synthesis and Metalation of Porphyrin Nanoparticles with Enanced Photocataylytic Performance. *Nano Lett.* **2016**, *16*, 6523−6528.

(56) Kiani, F. A.; Shamraiz, U.; Badshah, A. Enhanced photo catalytic activity of Ag$_2$O nanostructures through strontium doping. *Mater. Res. Express* **2020**, *7*, 015035.

(57) Adeel, M.; Saeed, M.; Khan, I.; Muneer, M.; Akram, N. Synthesis and characterization of Co−ZnO and evaluation of its photocatalytic activity for photodegradation of methyl orange. *ACS Omega* **2021**, *6*, 1426−1435.

(58) Kite, S. V.; Kadam, A. N.; Sathe, D. J.; Patil, S.; Mali, S. S.; Hong, C. K.; Lee, S. W.; Garadkar, K. M. Nanostructured TiO$_2$ sensitized with MoS$_2$ nanoflowers for enhanced photodegradation efficiency toward methyl orange. *ACS Omega* **2021**, *6*, 17071−17085.

(59) Gligorovski, S.; Strekowski, R.; Barbati, S.; Vione, D. Environmental Implications of Hydroxyl Radicals (●OH). *Chem. Rev.* **2015**, *115*, 13051−13092.

(60) Sheikh, M. U. D.; Naikoo, G. A.; Thomas, M.; Bano, M.; Khan, F. Solar-assisted photocatalytic reduction of methyl orange azo dye over porous TiO$_2$ nanostructures. *New J. Chem.* **2016**, *40*, 5483−5494.

(61) Wang, H.; Zhang, J.; Yuan, X.; Jiang, L.; Xia, Q.; Chen, H. Photocatalytic removal of antibiotics from natural water matrices and swine wastewater via Cu(I) coordinately polymeric carbon nitride framework. *Chem. Eng. J.* **2020**, *392*, 123638.

(62) Subhiksha, V.; Kokilavani, S.; Khan, S. S. Recent advances in degradation of organic pollutant in aqueous solutions using bismuth based photocatalysts: A review. *Chemosphere* **2022**, *290*, 133228.

(63) Ong, W. J.; Tan, L. L.; Ng, Y. H.; Yong, S. T.; Chai, S. P. Graphitic Carbon Nitride (g-C$_3$N$_4$)-Based Photocatalysts for Artificial Photo-synthesis and Environmental Remediation: Are We a Step Closer to Achieving Sustainability. *Chem. Rev.* **2016**, *116*, 7159−7329.